IOP Publishing Plasma Physics and Controlled Fusion

Plasma Phys. Control. Fusion **60** (2018) 044007 (8pp) https://doi.org/10.1088/1361-6587/aaacc2

Transverse phase space diagnostics for ionization injection in laser plasma acceleration using permanent magnetic quadrupoles

F Li[1], Z Nie[1], Y P Wu[1], B Guo[1], X H Zhang[1], S Huang[1], J Zhang[1], Z Cheng[1], Y Ma[1], Y Fang[1], C J Zhang[2], Y Wan[1], X L Xu[2,3], J F Hua[1], C H Pai[1], W Lu[1] and W B Mori[2]

[1] Department of Engineering Physics, Tsinghua University, Beijing 100084, People's Republic of China
[2] University of California Los Angeles, Los Angeles, CA 90095, United States of America
[3] SLAC National Accelerator Laboratory, Menlo Park, CA 94025, United States of America

E-mail: jfhua@tsinghua.edu.cn

Received 21 November 2017, revised 24 January 2018
Accepted for publication 2 February 2018
Published 22 February 2018

Abstract

We report the transverse phase space diagnostics for electron beams generated through ionization injection in a laser-plasma accelerator. Single-shot measurements of both ultimate emittance and Twiss parameters are achieved by means of permanent magnetic quadrupole. Beams with emittance of μm rad level are obtained in a typical ionization injection scheme, and the dependence on nitrogen concentration and charge density is studied experimentally and confirmed by simulations. A key feature of the transverse phase space, matched beams with Twiss parameter $\alpha_T \simeq 0$, is identified according to the measurement. Numerical simulations that are in qualitative agreement with the experimental results reveal that a sufficient phase mixing induced by an overlong injection length leads to the matched phase space distribution.

Keywords: emittance, phase space, Twiss parameter, permanent magnetic quadrupole, laser plasma accelerator

(Some figures may appear in colour only in the online journal)

1. Introduction

Laser plasma accelerators (LPAs) [1–3] can generate GeV electron bunches within centimeter-scale distance [4–10], which makes it promising candidate for the future compact light sources [11, 12] and linear colliders [13]. Besides sufficiently high beam energy, these LPA-based applications also have strict demand for the beam qualities, i.e. high current, low transverse emittance and narrow energy spread.

In order to obtain the desired high-quality beams, controllable particle injection must be achieved in the micron-class and highly transient plasma wake. As an important controllable injection method, ionization injection [6, 7, 14–17] has been proposed for years and are considered highly controllable and flexible. However, it is still challenging to generate high quality beams in such injection schemes because of the complex dynamics therein. One of those is the phase mixing [18] which has been proved to be responsible for the rapid emittance growth. Due to this effect, the accelerated beams tend to have a matched transverse phase space. This feature can be easily witnessed in simulations but not yet reported in any LPA experiment till now, because most of the existing diagnostics of LPA only allow emittance measurement but not characterization of transverse phase space. Radiation-based methods [12, 19–21] work depending on some assumptions like matched phase space or theoretical trajectory of betatron oscillation in the plasma wake. They can estimate the beam emittance inside the plasma wake but not that exiting the accelerator due to the emittance evolution within the plasma-vacuum transition. Although complete

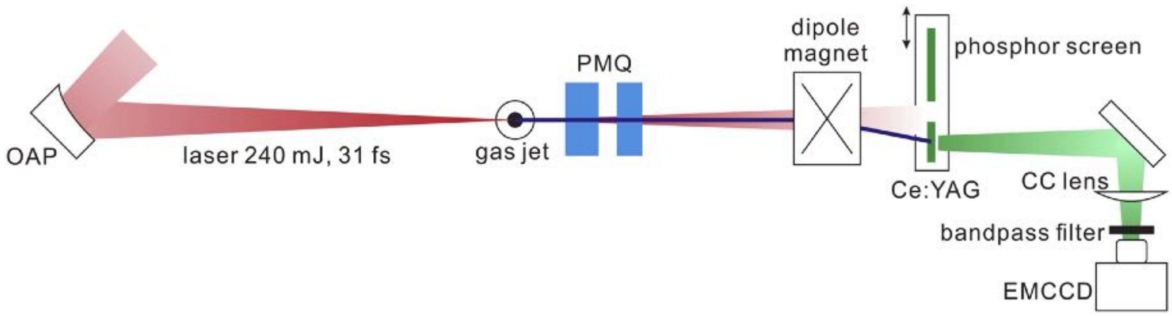

Figure 1. Schematic of the experimental setup. The laser pulse is focused by an off-axis parabola into a helium gas jet mixed with nitrogen. The out-coming electron beams are transported and focused by the PMQ doublet. After passing through the dipole magnet, the energy-resolved beams are collected by the detection screen.

phase space distribution can be retrieved, miniature pepper-pot method [22, 23] has been proved to be inaccurate for LPA beams [24]. In our point view, high-gradient permanent magnetic quadrupoles (PMQs) would be a good candidate due to the less limitations and assumptions compared with others. Different from miniature pepper-pot, it is essentially an un-blocking method with much higher electron throughput and thus allows low charge measurement. It also has the capability for measuring beams with μm-class transverse size. In contrast to radiation-based methods, one does not have to assume a matched phase space. With this method, not only the emittance but also the Twiss parameters [25], which describe the key features of transverse phase space, can be determined. Recently, emittance measurement [26, 27] and comparison study of different injection schemes [28] have been demonstrated experimentally using this method, and the feasibility for low emittance measurement of LPA beams has been confirmed in our previous work [29].

In the paper, we use PMQ method to characterize the transverse phase space of beams generated from ionization injection for different charge densities. Strong evidences indicate that matched electron beams have been generated in such LPA setup. Combining the particle-in-cell (PIC) simulations, the phase mixing is considered to result in the matched phase space. The emittance dependence on beam charge density obtained from the experimental data can be also well understood by simulations.

This paper is organized as follows: section 2 briefly introduces the experimental setup. In section 3, we report the generation of stable electron beams in ionization injection, and present the relevant beam parameters. Section 4 compares the measured emittance for different nitrogen concentrations and beam charge density by means of PMQ method. The transverse phase space is discussed in this section by use of the measured Twiss parameters. In section 5, we perform PIC simulations to have a deeper insight into the physics of ionization injection. Conclusions are drawn in the last section.

2. Experimental setup

The experiments were carried out at the laser wakefield acceleration platform at Tsinghua University [30]. Figure 1 shows the experimental setup. The 800 nm laser system delivered 400 mJ (on target) pulses of 31 fs FWHM duration polarized in x-plane. The laser pulses were focused by an $f/9.6$ off-axis parabola into a helium gas jet mixed with nitrogen. The focal plane was at the density upramp of the 2.9 mm long plasma source. The beam transport line following the plasma source was composed of a PMQ doublet and dipole magnet. The PMQs with aperture of 6 mm have field gradients of 284 T m^{-1} and 199 T m^{-1}, and effective lengths of 19.6 mm and 14.9 mm respectively. As the beam energy of most shots are around 55 MeV in the experiment, the beam-line setup is designed to focus beams of such energy, and can be uniquely determined by fixing the total length and requiring imaging the beams in both x- and y-planes (this point will be elaborated in section 4). As a result, the PMQs were placed 4.5 cm behind the plasma source. The interval between the PMQs was 3.7 cm. From the exit of the PMQ doublet, the beams drifted about 54 cm to reach the detection screen.

During the drift, they were bent by the dipole magnet which was placed 5 cm before the detection screen. A phosphor screen (PI200) was used to measure beam profiles and energy spectra, while a Ce:YAG crystal (300 μm thickness), which has much better spatial resolution, to observe the energy-resolved beam size for emittance measurement. Since the scintillation yield of a Ce:YAG crystal is much lower, an EMCCD camera was employed to increase the detection efficiency and signal-to-noise ratio.

PMQ method requires accurate measurement for the energy-resolved beam sizes and thus the spatial resolution of the detection system need to be carefully calibrated. There are primarily three factors blurring the captured images: imperfection of optical imaging system, multiple Coulomb scattering of electrons in the YAG crystal and the depth-of-field blurring. The point spread function (PSF) of the optical imaging system was characterized by using an USAF 1951 resolution target and the rms width of PSF σ_o was measured to be 12 μm. The rms widths of the equivalent PSF caused by the latter two factors were estimated to be $\sigma_s = 3.1$ μm and $\sigma_f = 21.6$ μm, respectively. Therefore the overall spatial resolution was $\sigma_{\text{tot}} = \sqrt{\sigma_o^2 + \sigma_s^2 + \sigma_f^2} = 25$ μm with which the image deconvolution was performed.

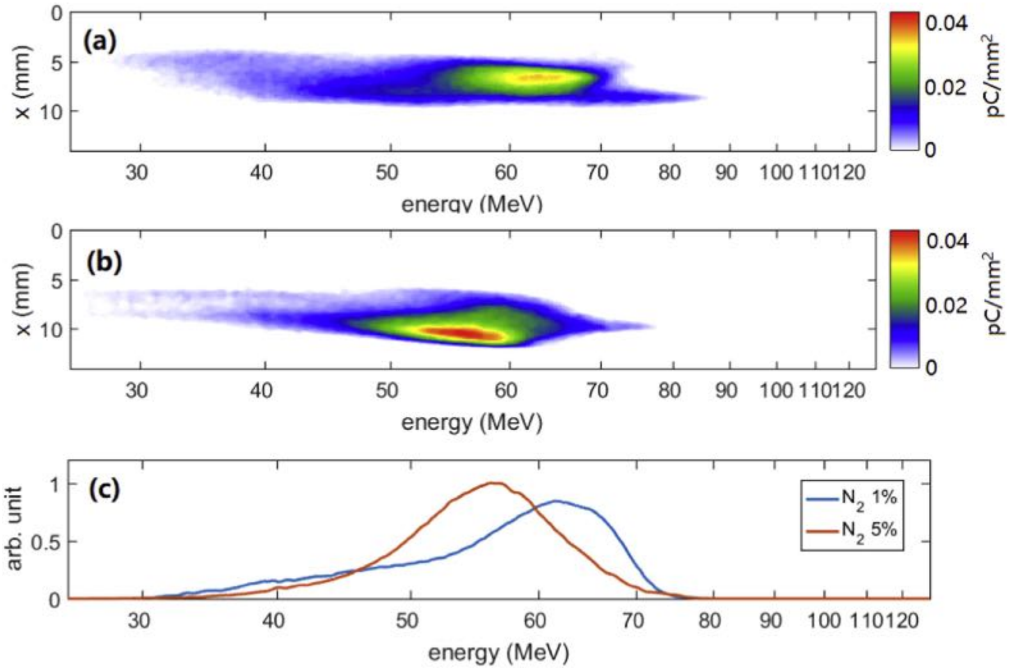

Figure 2. Typical signals on the energy spectrometer screen for (a) 1% and (b) 5% nitrogen concentrations. (c) The normalized energy spectra for the two nitrogen concentrations.

3. Stable electron beams generation in ionization injection

Typical ionization injection utilizes mixed gas with the low-*Z* component providing the background plasma electrons and the high-*Z* component serving as the injection source. Here, a helium–nitrogen gas jet was used in our LPA experiments with the nitrogen concentration of 1% and 5%. For both cases, the plasma density contributed by the helium electrons and outermost five electrons of nitrogen was 3.5×10^{18} cm^{-3}, at which the injection probability and parametric stability were optimized. We used the PI-200 phosphor screen to characterize the beam profiles and the energy spectra. Using the calibration of charge-photon conversion for PI-200 [31] and assuming the photon emission obeys Lambertian cosine law, the beam charge was estimated by calculating the total CCD counts. Typical measured energy spectra are shown in figure 2. By optimizing the LPA, stable electron beams were delivered with average energies of 62 MeV and 51 MeV (consecutive 50 shots) for the 1% and 5% nitrogen concentrations respectively. The rms energy spreads were 20% and 36% containing average charges of 10.0 ± 1.4 pC and 17.2 ± 3.7 pC for the two cases.

The beams were focused by the PMQ doublet, which not only reduces the beam size but also the transverse position fluctuation significantly [32]. By counting successive 50 shots, the free-drifting transverse position fluctuations were 2.4×1.4 mm and 3.0×1.8 mm for 1% and 5% nitrogen concentrations respectively, while they were reduced to 0.5×0.5 mm and 0.1×0.6 mm after focusing. The beam position distributions are shown in figure 3. After focusing,

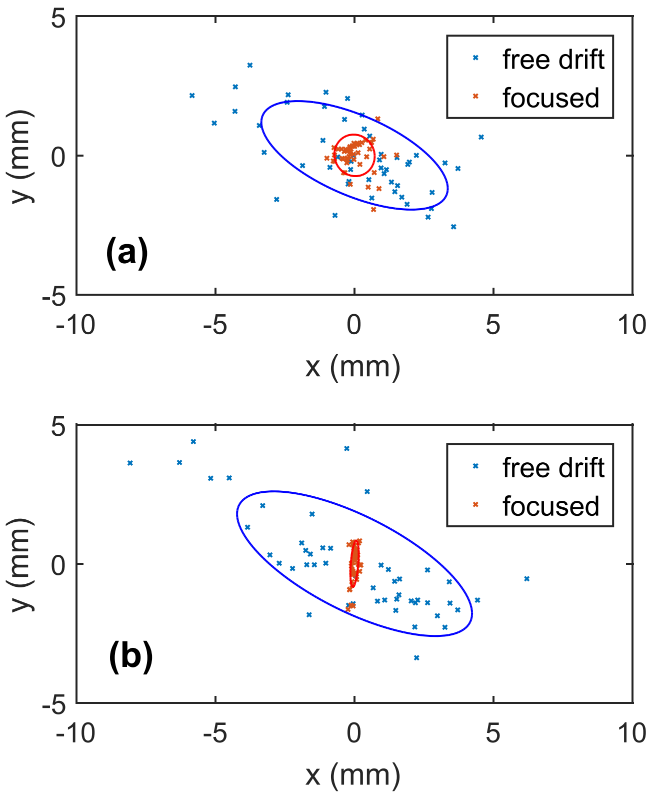

Figure 3. Transverse position fluctuation of the free drifting and focused electron beams. Beam spot positions for (a) 1% and (b) 5% nitrogen concentrations on the PI200 screen. The area enclosed by the ellipses denotes the rms position fluctuation for the free drifting (blue) and focused beams (red).

the position stability was improved by 10 and 70 times (comparing the area of ellipses) for 1% and 5% nitrogen concentrations respectively.

Because of the focusing by PMQs, the transverse beam position stabilization can be much improved and therefore the accuracy of spectrum diagnostics. We have measured the charge after focusing, and found only around 30% were finally captured by the screen. This is because a large energy spread leads to those electrons deviating much from the central energy cannot be well focused and thus form a large background on the detection screen. Nonetheless, according to the discussion on the energy-emittance relevance in [29], retrieving the emittance by using only a fraction of electrons is still considered to be reasonable and sufficiently precise.

4. Emittance measurement and transverse phase space characterization

After passing through the dipole magnet, the focusing energy-resolved beam size σ_x becomes a function of energy E. Considering the linear beam optics, the phase space is determined by the transport matrix, i.e. $(x, x')^{\mathrm{T}} = \mathbf{M}(x_0, x_0')^{\mathrm{T}}$. The energy-resolved beam size is therefore expressed as

$$\sigma_x(E) = \sqrt{M_{x,11}^2(\beta_{\mathrm{T}}\epsilon_x) + M_{x,12}^2(\gamma_{\mathrm{T}}\epsilon_x) - 2M_{x,11}M_{x,12}(\alpha_{\mathrm{T}}\epsilon_x)}, \tag{1}$$

where $M_{ij}(E)$ are the elements of $\mathbf{M}$ and are functions of E. The initial Twiss parameters β_{T}, γ_{T}, α_{T} characterize the phase space. For an optimized beam-line, the central energy E_0 minimizes $\sigma_x(E)$ while the fraction deviating from E_0 has a larger σ_x. Therefore the signal on the detection screen usually appears like a 'bow-tie' shape after dispersed by the dipole magnet, which allows single-shot measurement through σ_x–E relation. For a PMQ doublet beam-line, the intervals between components can be uniquely determined by three constraints. Two of them are the imaging requirements in both x and y directions for the central energy E_0, i.e. $M_{x,12}(E_0) = M_{y,12}(E_0) = 0$, while the other one is determined by the practical experiment layout, i.e. the beam-line length. After determining the lattice parameters, the resultant magnification of the beam optics imaging system is found to be ~20 which is considered to be enough for the beam size resolution. Since the Ce:YAG crystal has a limited area ($1 \times 1.5\,\mathrm{cm}^2$), only the beam size within a narrow bandwidth ± 1 MeV around E_0 can be observed. However, retrieving the emittance using only part of beams, as mentioned above, is sufficiently accurate.

The PMQ method can not only measure the emittance but also Twiss parameters that characterize the phase space. From equation (1), $(\beta_{\mathrm{T}}\epsilon_x)$, $(\alpha_{\mathrm{T}}\epsilon_x)$ and $(\gamma_{\mathrm{T}}\epsilon_x)$ (the products in the brackets are considered as a whole) can be determined by fitting $\sigma_x(E)$. Using the well-known relation $\beta_{\mathrm{T}}\gamma_{\mathrm{T}} - \alpha_{\mathrm{T}}^2 \equiv 1$, Twiss parameters can be obtained by $\beta_{\mathrm{T}} = (\beta_{\mathrm{T}}\epsilon_x)/\epsilon_x$, $\alpha_{\mathrm{T}} = (\alpha_{\mathrm{T}}\epsilon_x)/\epsilon_x$ and $\gamma_{\mathrm{T}} = (\gamma_{\mathrm{T}}\epsilon_x)/\epsilon_x$, where the measured emittance ϵ_x is derived from $\epsilon_x = \sqrt{(\beta_{\mathrm{T}}\epsilon_x)(\gamma_{\mathrm{T}}\epsilon_x) - (\alpha_{\mathrm{T}}\epsilon_x)^2}$.

Following the discussions on several error sources in our previous work, we carefully considered the impacts of the azimuthal angular errors and the high-order field components (HOFC) of PMQs. The measurement precision is mostly sensitive to the azimuthal angular errors of PMQs which will cause astigmatic focusing and overestimation for $\sigma_x(E)$. To minimize this uncertainty, the offset between the machining center and the magnetic field center was carefully characterized, and the beam-line was carefully aligned as well. By doing this, the azimuthal angular rotation was controlled within 0.3° which induces ~20% overestimation [29] for the measured emittance at most. The HOFC is usually regarded as an insensitive factor for measurement. However, it could become non-ignorable when the bore of PMQ is relatively small because of the HOFCs' dependence on ρ^l, where ρ is the radial position and l the order of HOFC. This indicates the beams with relatively large transverse size suffer more significant nonlinear effect induced by HOFCs. In order to estimate such uncertainty, we imported the measured HOFCs and simulated $\sigma_x(E)$ for the measured initial Twiss parameters and emittances. It was found that, for our magnets, the emittance overestimation caused by HOFCs is controlled within 5%. Other non-ideal factors in experiments like the transverse position misalignment of beam-line and the beam pointing jitter are proved to have very modest impacts on the emittance measurement.

There are three types of error needed to be considered for the measured emittance. The first is the systematic error caused by PMQ azimuthal angular uncertainty and HOFCs as aforementioned. This can be directly estimated according to [29]. The second type is caused by the ambiguity of defining the beam size when fitting the distribution for each energy slice. To avoid this, a threshold was set and only the profile above it was involved in the fit, which can effectively reduce the impact from the peripheral signals or background noise. The emittance was calculated using the fitted $\sigma_x(E)$ with a threshold 30% of the peak value, while the upper and lower limit (the vertical error bars in figure 5) were determined with thresholds of 10% and 50%. The last one is the signal fluctuation contributed by the background noise which is denoted by the error shades in figure 4(b). The total error is the uncorrelated combination of these three types. Figure 4(a) shows the typical image captured by the Ce:YAG screen for 5% nitrogen concentration. The energy-resolved beam sizes for each energy slice, as denoted by the solid lines in figure 4(b), were obtained by Gaussian fit. The two shots shown in figure 4(b) are $3.1^{+0.8}_{-0.7}\,\mu$m rad (1% nitrogen) and $9.3^{+1.6}_{-1.0}\,\mu$m rad (5% nitrogen), respectively. Here, the systematic errors are estimated to be 0.7 μm rad and 0.9 μm rad, respectively.

Figure 5 shows the measured emittance from consecutive 50 shots for each nitrogen concentration. Among those shots, the minimum measured emittance is $2.5^{+0.4}_{-0.2}\,\mu$m rad. The results show no essentially distinction between different nitrogen concentrations, but the emittances present roughly increasing trend with increasing charge density. Below 0.3 pC MeV^{-1} the measured emittances are within the range from 2.5 to 5 μm rad without significant correlation between the emittance and charge density. When exceeding 0.3 pC MeV^{-1}, the measured emittance grows rapidly with

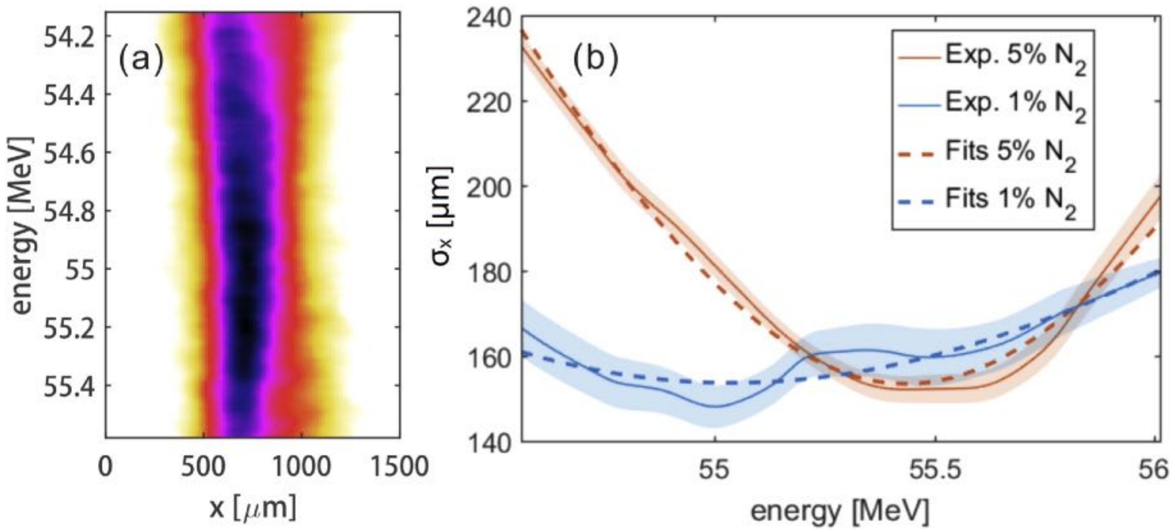

Figure 4. (a) The typical 'bow-tie' image on the Ce:YAG screen for 5% nitrogen concentration. The beam is dispersed in y-direction and $\sigma_x(E)$ is calculated for each row of the image. (b) The energy-resolved beam size versus energy for 1% (blue solid line) and 5% (red solid line) nitrogen concentrations. The shades denote the fluctuation of $\sigma_x(E)$ around its average values. The dashed lines are the fits to equation (1).

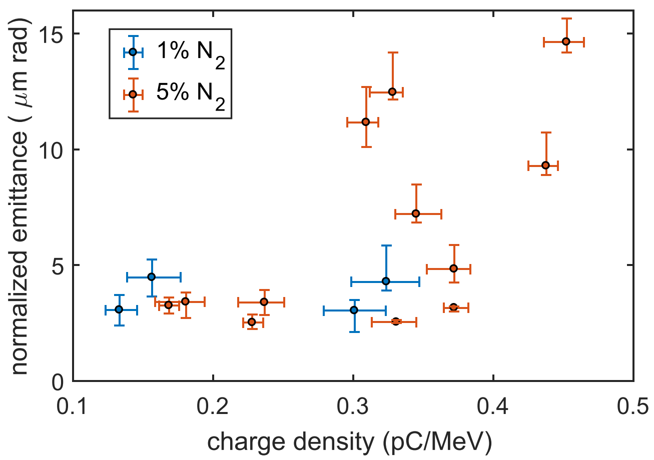

Figure 5. Emittance versus energy-related charge density. Each point is calculated by determining $\sigma_x(E)$ with Gaussian fitting the slice beam profile above the threshold of 30% of the peak value. The error bars are determined using the thresholds of 10% and 50%. For the vertical error bars, the fluctuations of $\sigma_x(E)$ around the average values (denoted by the shades in figure 4(b)) are also involved. The horizontal error bars are estimated by integrating the fitting profiles of thresholds 10% and 50% within interval $(-\sigma_x, +\sigma_x)$ at E_0.

increasing charge density. We note that this trend would not be caused by space charge effect as reported in [28] in which the charge density is much higher, but rather probably by the undesired injection in the second bucket of the wake. This point will be discussed in detail in the following section. As a deduction, the beam emittance for low charge density is mainly contributed by the electron trapped in the first bucket, and is estimated to be $3.3 \pm 0.6\ \mu$m rad using the measured data below 0.3 pC MeV^{-1}. This deduction can be also qualitatively verified by simulations in the next section.

We measured the Twiss parameters and found that α_T for all the measurements almost vanishes, which can be justified by the β_T–γ_T relation shown in figure 6(a). It can be seen that all the points reside very closed to the line $\beta_T\gamma_T = 1$, which implies $\alpha_T \approx 0$ recalling that $\beta_T\gamma_T - \alpha_T^2 \equiv 1$. The vanishing of α_T indicates that the distribution of x_0 decouples from that of x_0', and therefore the phase space (x_0, x_0') appears like a canonical ellipse, as shown in figure 6(b) in which two determined phase ellipses are plotted corresponding to the points marked by arrows in figure 6(a). They show the biggest difference in the aspect ratio of the measured phase ellipses. There are two possibilities for the formation of a nearly canonical phase ellipse: (i) the electron beams exit the plasma at their beam waist or anti-waist. (ii) the beam is matched so that $\alpha_T = 0$ is always satisfied during the acceleration. The first inference is easy to be negated because it is unlikely for all the measured beams emitting from the plasma exactly right at their waist or anti-waist. In fact, we tried to change the betatron oscillation phase of the beams at the exit by changing the focal plane of laser pulses in the experiments, but no significant difference for α_T was observed, which once again implies the second inference. We note that a typical ionization injection triggered by a single laser pulse is apt to produce matched electron beams due to the relatively long injection distance [18]. Our experimental results verify this point well.

5. Numerical simulation

We carried out full 3D PIC simulations using code OSIRIS [33–35] to qualitatively compare the ionization injection for different nitrogen concentrations. To obtain convincing simulation results, a specified algorithm [36] was used to suppress the numerical Cerenkov instability which would give rise to spurious emittance growth. With the typical experimental parameters, the PIC simulations reveal the distinction in the injection process for different laser-plasma parameters.

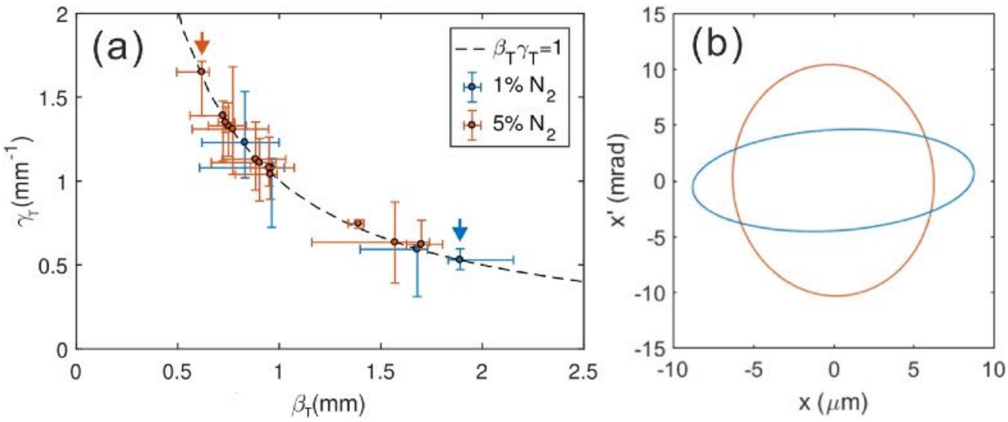

Figure 6. (a) Measured β_T versus γ_T. Each point is calculated by determining $\sigma_x(E)$ with Gaussian fitting the slice beam profile above the threshold of 30% of the peak value. The error bars are determined using the thresholds of 10% and 50%, coupling with the fluctuations of $\sigma_x(E)$ (denoted by the shades in figure 4(b)). (b) Phase ellipses corresponding to the points marked by arrows in (a).

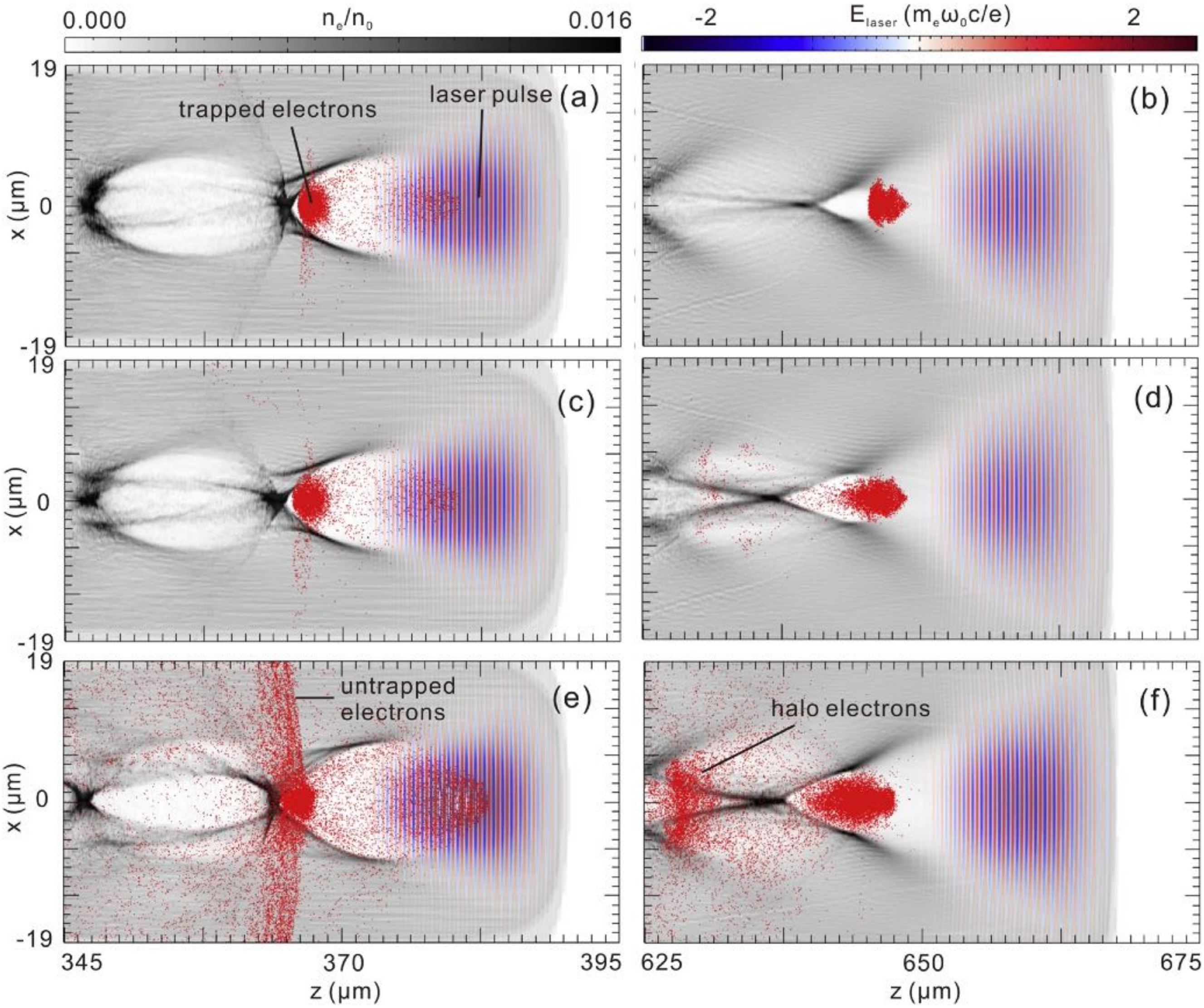

Figure 7. Simulation snapshots of injection process at different time for (a), (b) $a_0 = 1.8$ and 1% nitrogen, (c) and (d) $a_0 = 1.8$ and 5% nitrogen, and (e), (f) $a_0 = 2.2$ and 5% nitrogen, respectively.

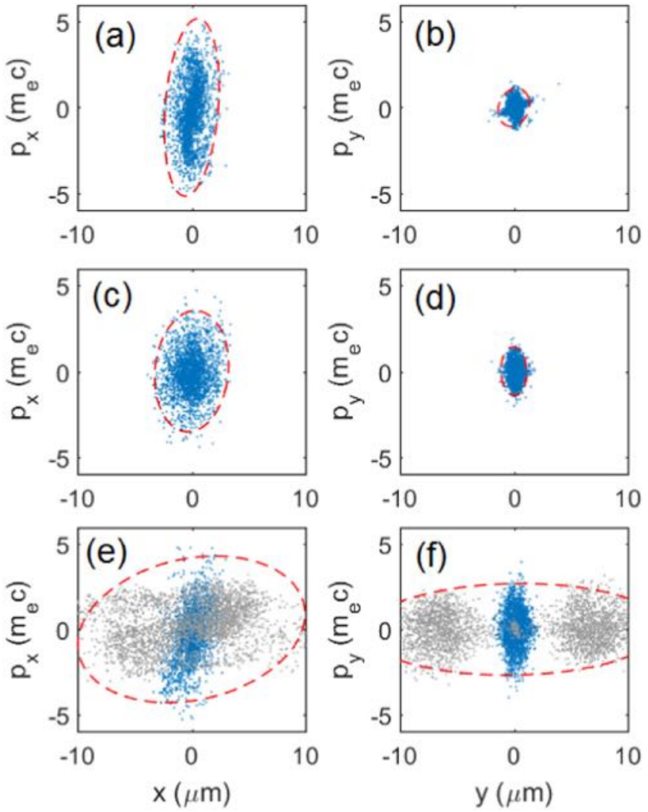

Figure 8. Transverse phase space distributions of x- and y-directions for (a), (b) $a_0 = 1.8$ and 1% nitrogen, (c) and (d) $a_0 = 1.8$ and 5% nitrogen, and (e), (f) $a_0 = 2.2$ and 5% nitrogen, respectively. The red dashed ellipses enclose 98% macro-particles with which the emittances are calculated. In subplots (e) and (f), the gray dots represent the particles trapped in the second bucket.

Simulation snapshots at different time are shown in figure 7. Figures 7(a) and (c) show the density distribution at $z = 370\ \mu$m where the particle injection is under way, for 1% and 5% nitrogen concentrations respectively. With peak laser intensity $a_0 = 1.8$, the blowout regime [37] is excited and a bubble-like plasma wake is formed. The red dots shown therein represent the ionized inner-shell electrons of nitrogen. The background plasma is composed of helium electrons and the five outermost electrons of nitrogen. It can be seen that the cases of different nitrogen concentrations, under the conditions close to our experimental setup, present no significant distinction during the injection. Majority of the ionized inner-shell electrons are eventually captured into the first bucket of the wake, as shown in figures 7(b) and (d) in which the injection has ceased. Despite the remarkable distinction in beam charge for both nitrogen concentrations (13 pC and 39 pC for 1% and 5% nitrogen concentrations respectively), there is no notable difference for the emittance ($\sim$1.2 μm rad for both) in x-direction as shown in figures 8(a) and (c). This is because the residue transverse momenta $p_{x,\mathrm{res}}$ are mainly modulated by the laser-beam interaction after ionization, which is roughly determined by the canonical momentum conservation $p_{x,\mathrm{res}} = p_{x0} - a_i m_e c$ where p_{x0} is the initial momenta after ionization which can be considered zero, and a_i the initial normalized vector potential of laser. The simulations qualitatively agree to the experimental results of charge density <0.3 pC MeV^{-1}. Notably, although not measured in our experiments, the emittances in the unpolarized direction of laser (y-direction) present obvious difference for both nitrogen concentrations, with 0.12 and 0.18 μm rad for 1% and 5% nitrogen respectively, as shown in figures 8(b) and (d). In this direction, the laser-beam interaction becomes much weaker and the space charge effect begins to influence the residue momenta $p_{y,\mathrm{res}}$, and therefore the ultimate emittance.

Table 1. α_T for the injected beams in the simulations. x- and y-directions refer to the polarized and unpolarized planes of laser, respectively.

	$a_0 = 1.8$, 1% N_2	$a_0 = 1.8$, 5% N_2	$a_0 = 2.2$, 5% N_2
x-direction	0.25	0.14	0.24
y-direction	0.15	−0.08	0.05

When increasing the laser intensity by 50%, the injection becomes quite different as shown in figures 7(e) and (f). In such circumstance, considerable ionized inner-shell nitrogen electrons are scattered and hence not get trapped in the first bucket. A fraction of these electrons are captured in the second bucket but have very large emittance, which resultantly form a big beam halo as the gray dots denote in figures 8(e) and (f). Owing to this, the emittance in x- and y-directions dramatically increase to 3.6 and 4.5 μm rad. The electron trapping occurring in the second bucket is quite stochastic and sensitive to laser-plasma parameters. Therefore, it can be used to interpret the significantly larger but random-looking measured emittance for charge density >0.3 pC MeV^{-1} in figure 5.

For all the phase space distributions in figure 8, the phase ellipses denoted by the red dashed lines resemble canonical ones, which indicates that all the beams are near-matched with very small α_T. We list α_T for both $a_0 = 1.8$ and $a_0 = 2.2$ cases in table 1 according to $\alpha_\mathrm{T} \equiv \langle uu' \rangle / \epsilon_{u,\mathrm{geo}}$, where u denotes x or y and $\epsilon_{u,\mathrm{geo}}$ is the geometry emittance. It can be seen that for all the simulation cases, $\alpha_\mathrm{T} \ll 1$ is satisfied, which is fully consistent with aforementioned experimental measurements. The underlying physics of matched beam generation can be uncovered by the simulations. It is found that the injection length L_inj, i.e. the distance from the birthplace of first injected electron to that of the last one, is very long so that the phase-mixing [18] is sufficiently developed, leading to a matched beam. The injection length derived from the simulations for $a_0 = 1.8$ is $L_\mathrm{inj} \sim 70 k_p^{-1} \gg \pi k_p^{-1}$, where k_p is plasma wavenumber corresponding to $n_p = 3.5 \times 10^{18}\ \mathrm{cm}^{-3}$. It implies that, when the injection terminates, the first group of ionized inner-shell nitrogen electrons have rotated through a couple of periods in the transverse phase space, forming a matched beam. For the case of $a_0 = 2.2$, L_inj becomes even longer, reaching $\sim 150 k_p^{-1}$. In fact, a matched beam is frequently obtained for a typical ionization injection geometry, i.e. the laser co-propagates with the wake, in simulations. In our previous work [38, 39], very high quality and mismatched beams can be obtained through ionization injection if using a specified geometry to limit the injection length. In this case, the evolution of phase space is much complicated and therefore the PMQ method would be of more value.

6. Conclusion

In conclusion, ionization injection LPA experiments have been carried out at Tsinghua University using its 30 TW laser system. Stable electron beams with average energy of 50–70 MeV were produced in a laser-ionized plasma formed by a helium gas jet doped with nitrogen. Using PMQ method, not only the ultimate emittances but also the Twiss parameters were measured. For low charge density, the measured emittances in the polarized direction of laser, with mean value of $\sim 3\ \mu$m rad, present no significant difference between 1% and 5% nitrogen concentrations. However, the measured emittances increase dramatically for high charge density and have a relatively random distribution. Simulations reveal that the second-bucket-injection contributes to the dramatical emittance growth as increasing charge density. The beams trapped in the first bucket have no essential distinction in emittance because it is dominated by the laser-beam interaction after ionization, which can be considered identical for different charge density and nitrogen concentrations. Experimental measurement also exhibits matched phase space distribution for all the injected beams, typically with $\alpha_T \sim 0$. This result was examined via simulations as well. With parameters similar to the experiment setup, it was found matched beams primarily stem from an overlong injection length, which allows the phase mixing to be sufficiently developed.

Acknowledgments

This work was supported by NSFC Grant No. 11425521, No. 11535006, No. 11775125, No. 11475101 and No. 11375006. The numerical simulations were carried out using Blue Waters cluster at National Center for Supercomputing Applications (NCSA) and Sunway TaihuLight cluster at National Supercomputing Center in Wuxi (NSCCWX).

ORCID iDs

F Li https://orcid.org/0000-0001-8627-910X
C J Zhang https://orcid.org/0000-0001-8035-3014
Y Wan https://orcid.org/0000-0001-6089-3718

References

[1] Tajima T and Dawson J M 1979 *Phys. Rev. Lett.* **43** 267
[2] Malka V *et al* 2002 *Science* **298** 1596–600
[3] Joshi C and Katsouleas T 2003 *Phys. Today* **56** 47–53
[4] Leemans W P, Nagler B, Gonsalves A J, Toth C, Nakamura K, Geddes C G R, Esarey E, Schroeder C B and Hooker S M 2006 *Nat. Phys.* **2** 696–9
[5] Kneip S *et al* 2009 *Phys. Rev. Lett.* **103** 035002
[6] Clayton C E *et al* 2010 *Phys. Rev. Lett.* **105** 105003
[7] Pollock B B *et al* 2011 *Phys. Rev. Lett.* **107** 045001
[8] Wang X *et al* 2013 *Nat. Commun.* **4** 1988
[9] Kim H T, Pae K H, Cha H J, Kim I J, Yu T J, Sung J H, Lee S K, Jeong T M and Lee J 2013 *Phys. Rev. Lett.* **111** 165002
[10] Leemans W P *et al* 2014 *Phys. Rev. Lett.* **113** 245002
[11] Schlenvoigt H P *et al* 2008 *Nat. Phys.* **4** 130–3
[12] Kneip S *et al* 2010 *Nat. Phys.* **6** 980–3
[13] Schroeder C B, Esarey E, Geddes C G R, Benedetti C and Leemans W P 2010 *Phys. Rev. Spec. Top.—Accel. Beams* **13** 101301
[14] McGuffey C *et al* 2010 *Phys. Rev. Lett.* **104** 025004
[15] Pak A, Marsh K A, Martins S F, Lu W, Mori W B and Joshi C 2010 *Phys. Rev. Lett.* **104** 025003
[16] Liu J S *et al* 2011 *Phys. Rev. Lett.* **107** 035001
[17] Vafaei-Najafabadi N *et al* 2014 *Phys. Rev. Lett.* **112** 025001
[18] Xu X L *et al* 2014 *Phys. Rev. Lett.* **112** 035003
[19] Plateau G R *et al* 2012 *Phys. Rev. Lett.* **109** 064802
[20] Schnell M *et al* 2012 *Phys. Rev. Lett.* **108** 075001
[21] Curcio A, Anania M, Bisesto F, Chiadroni E, Cianchi A, Ferrario M, Filippi F, Giulietti D, Marocchino A and Petrarca M 2017 *Phys. Rev. Accel. Beams* **20** 012801
[22] Fritzler S, Lefebvre E, Malka V, Burgy F, Dangor A E, Krushelnick K, Mangles S P D, Najmudin Z, Rousseau J P and Walton B 2004 *Phys. Rev. Lett.* **92** 165006
[23] Brunetti E *et al* 2010 *Phys. Rev. Lett.* **105** 215007
[24] Cianchi A *et al* 2013 *Nucl. Instrum. Methods Phys. Res.* A **720** 153–6
[25] Lee S Y 2004 *Accelerator Physics* 2nd edn (Singapore: World Scientific)
[26] Weingartner R *et al* 2012 *Phys. Rev. Spec. Top.—Accel. Beams* **15** 111302
[27] Vafaei-Najafabadi N *et al* 2016 *Plasma Phys. Control. Fusion* **58** 034009
[28] Barber S K *et al* 2017 *Phys. Rev. Lett.* **119** 104801
[29] Li F *et al* 2018 *Plasma Phys. Control. Fusion* **60** 014029
[30] Jian-Fei H *et al* 2015 *Chin. Phys.* C **39** 17001–7
[31] Wu Y C, Zhu B, Dong K G, Yan Y H and Gu Y Q 2012 *Rev. Sci. Instrum.* **83** 026101
[32] Weingartner R *et al* 2011 *Phys. Rev. Spec. Top.—Accel. Beams* **14** 052801
[33] Fonseca R *et al* 2002 *OSIRIS: A Three-Dimensional, Fully Relativistic Particle in Cell Code for Modeling Plasma Based Accelerators* (*Lecture Notes in Computer Science* vol 2331) (Berlin: Springer) pp 342–51
[34] Fonseca R A, Martins S F, Silva L O, Tonge J W, Tsung F S and Mori W B 2008 *Plasma Phys. Control. Fusion* **50** 124034
[35] Fonseca R A, Vieira J, Fiuza F, Davidson A, Tsung F S, Mori W B and Silva L O 2013 *Plasma Phys. Control. Fusion* **55** 124011
[36] Li F *et al* 2017 *Comput. Phys. Commun.* **214** 6–17
[37] Lu W, Huang C, Zhou M, Mori W B and Katsouleas T 2006 *Phys. Rev. Lett.* **96** 165002
[38] Li F *et al* 2013 *Phys. Rev. Lett.* **111** 015003
[39] Xu X L *et al* 2014 *Phys. Rev. Spec. Top.—Accel. Beams* **17** 061301